

Search for Invisible Axion Dark Matter in the 3.3–4.2 μeV Mass Range

C. Bartram,¹ T. Braine,¹ E. Burns,¹ R. Cervantes,¹ N. Crisosto,¹ N. Du,¹ H. Korandla,¹ G. Leum,¹ P. Mohapatra,¹ T. Nitta,^{1,*} L. J. Rosenberg,¹ G. Rybka,¹ J. Yang,¹ John Clarke,² I. Siddiqi,² A. Agrawal,³ A. V. Dixit,³ M. H. Awida,⁴ A. S. Chou,⁴ M. Hollister,⁴ S. Knirck,⁴ A. Sonnenschein,⁴ W. Wester,⁴ J. R. Gleason,⁵ A. T. Hipp,⁵ S. Jois,⁵ P. Sikivie,⁵ N. S. Sullivan,⁵ D. B. Tanner,⁵ E. Lentz,⁶ R. Khatiwada,^{7,4} G. Carosi,⁸ N. Robertson,⁸ N. Woollett,⁸ L. D. Duffy,⁹ C. Boutan,¹⁰ M. Jones,¹⁰ B. H. LaRoque,¹⁰ N. S. Oblath,¹⁰ M. S. Taubman,¹⁰ E. J. Daw,¹¹ M. G. Perry,¹¹ J. H. Buckley,¹² C. Gaikwad,¹² J. Hoffman,¹² K. W. Murch,¹² M. Goryachev,¹³ B. T. McAllister,¹³ A. Quiskamp,¹³ C. Thomson,¹³ and M. E. Tobar¹³

(ADMX Collaboration)

¹University of Washington, Seattle, Washington 98195, USA²University of California, Berkeley, California 94720, USA³University of Chicago, Illinois 60637, USA⁴Fermi National Accelerator Laboratory, Batavia, Illinois 60510, USA⁵University of Florida, Gainesville, Florida 32611, USA⁶University of Göttingen, Göttingen 37077, Germany⁷Illinois Institute of Technology, Chicago, Illinois 60616, USA⁸Lawrence Livermore National Laboratory, Livermore, California 94550, USA⁹Los Alamos National Laboratory, Los Alamos, New Mexico 87545, USA¹⁰Pacific Northwest National Laboratory, Richland, Washington 99354, USA¹¹University of Sheffield, Sheffield S3 7RH, United Kingdom¹²Washington University, St. Louis, Missouri 63130, USA¹³University of Western Australia, Perth, Western Australia 6009, Australia

(Received 11 October 2021; accepted 16 November 2021; published 23 December 2021)

We report the results from a haloscope search for axion dark matter in the 3.3–4.2 μeV mass range. This search excludes the axion-photon coupling predicted by one of the benchmark models of “invisible” axion dark matter, the Kim-Shifman-Vainshtein-Zakharov model. This sensitivity is achieved using a large-volume cavity, a superconducting magnet, an ultra low noise Josephson parametric amplifier, and sub-Kelvin temperatures. The validity of our detection procedure is ensured by injecting and detecting blind synthetic axion signals.

DOI: [10.1103/PhysRevLett.127.261803](https://doi.org/10.1103/PhysRevLett.127.261803)

In the Standard Model of particle physics, the amount of charge-parity (CP) violation by the strong interactions is set by an angle θ whose value is expected to be of order one [1]. However, the upper limit on the neutron electric dipole moment [2] requires $\theta < 5 \times 10^{-11}$. This discrepancy is called the strong- CP problem. The existence of a new global axial $U(1)$ symmetry, proposed by Peccei and Quinn (PQ) [3], would solve the strong- CP problem. This symmetry must be spontaneously broken, implying the existence of a pseudo Nambu-Goldstone boson, called the

axion [3–5]. The relic axions produced during the QCD phase transition in the early Universe [6–8] satisfy all the requirements of dark matter [9]. Thus the hypothetical axion solves both the strong- CP and dark matter problems. In the scenario in which the PQ symmetry breaks before cosmological inflation (preinflationary scenario), the relic axion abundance is determined only by the initial amplitude (θ_0) and mass of the axion field. The abundance of dark matter in the Lambda cold dark matter model is naturally explained by an axion mass above $\sim 0.1 \mu\text{eV}$ for $\theta_0 > 0.1$ [10,11]. In the postinflationary scenario, where the PQ symmetry breaks after cosmological inflation, most calculations suggest that the axion mass lies in the $\mathcal{O}(1-100) \mu\text{eV}$ range [10–22]. The axion has a coupling to two photons, and the numerical values are represented by two benchmark models, the Kim-Shifman-Vainshtein-Zakharov (KSVZ) [23,24] and Dine-Fischler-Srednicki-Zhitnitsky (DFSZ) [25,26] models.

Published by the American Physical Society under the terms of the [Creative Commons Attribution 4.0 International license](https://creativecommons.org/licenses/by/4.0/). Further distribution of this work must maintain attribution to the author(s) and the published article's title, journal citation, and DOI. Funded by SCOAP³.

Since those axion-photon couplings are expected to be small, $\mathcal{O}(10^{-17}\text{--}10^{-12}) \text{ GeV}^{-1}$, axions predicted by the models are called “invisible” axions [27].

To date, only the Axion Dark Matter eXperiment (ADMX) [28–33] has attained a sensitivity to the DFSZ model, which is a particularly well-motivated model because it can be grand unified. ADMX is a haloscope experiment [1,27,34] searching for axions within the local halo with a cold resonant cavity immersed in a static magnetic field. Maxwell’s equations modified to include the axion-photon interaction imply that an oscillating axion field (ϕ) in a static magnetic field (\vec{B}) induces an oscillating electric current, $\vec{j}_a = g_{a\gamma\gamma} \vec{B} \partial_t \phi$, where $g_{a\gamma\gamma}$ is the coupling of the axion to two photons. The electric current \vec{j}_a oscillates with a frequency E/h , where E is the sum of the mass (m) and kinetic energy of dark matter axions and h is the Planck’s constant. $E/h \approx mc^2/h$ because halo axions are nonrelativistic. The induced currents resonantly drive electromagnetic modes of the cavity with a resonant frequency equal to the frequency E/h of axion field oscillations. This signal is extracted by an antenna, amplified by several amplifiers, and sampled by a digitizer. Because the power from the axion signal is extremely small due to the minuscule axion-photon coupling, physical temperatures, and electronic noise from the amplifiers need to be as low as possible.

Previous reports by the ADMX collaboration have excluded masses over $2.7\text{--}3.3 \mu\text{eV}$ for the DFSZ model [32,33]. This Letter reports results of the search for axions in the $3.3\text{--}4.2 \mu\text{eV}$ mass range.

The ADMX experimental apparatus consists of a 136ℓ cylindrical copper-plated stainless steel microwave cavity in a 7.5 T superconducting magnet. Two movable bulk copper rods inside the cavity tune its resonant frequency. A variable depth antenna at the top of the cavity picks up rf signals inside the cavity. The coupling to the cavity is kept in a critically or overcoupled state by varying the insertion depth of the antenna to maximize the sensitivity to axion signals. A simplified rf diagram for the ADMX apparatus is shown in Fig. 1. The rf signals extracted from the cavity pass through two circulators and are amplified by the first stage amplifier, a Josephson parametric amplifier (JPA) [35]. The JPA achieves parametric amplification using the four-wave mixing produced by the nonlinearity of its SQUID (superconducting quantum interference device) loops. The JPA exhibits ultralow noise performance, just above the quantum limit, by adding noise only from the thermal population of the mode at the idler frequency [36]. The JPA is operated in a phase-preserving mode with a static current run through a nearby flux loop to bias the SQUIDs and a pump tone offset by 300 kHz from the resonant frequency of the cavity. Because the circulators and the JPA are sensitive to external magnetic fields, they are placed in a magnetic-field-free region generated by a

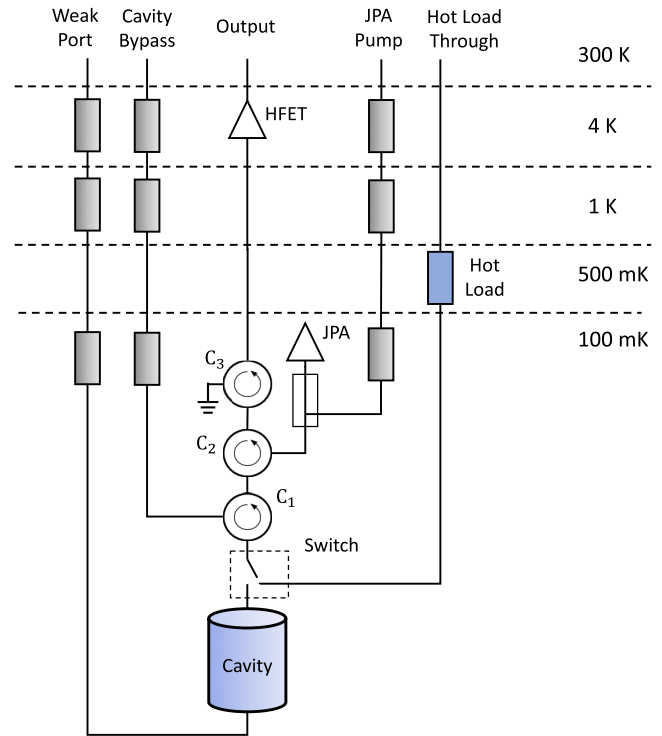


FIG. 1. The ADMX rf diagram. C_1 , C_2 , and C_3 are circulators. The JPA is connected with a pump power line via a directional coupler. The gray-colored rectangular boxes denote cryogenic attenuators. The switch is connected to the cavity during data taking, the bypass for the hot load is used for system noise calibrations.

bucking coil magnet designed to cancel the stray magnetic field from the main superconducting magnet. Empirically, we found that for a fixed bucking coil current, variations smaller than 0.2 A in the main magnet produced no significant changes in the JPA performance. Additionally, the JPA is inside a three-layer μ -metal shield to attenuate any remaining fields. By fine-tuning the bias current and pump power, we achieved a power gain of 15–30 dB across the frequency range. Amplified rf signals propagate through two circulators and are further amplified by the second stage amplifier, a heterostructure field effect transistor amplifier, model number LNF-LNC0.6_2A [37], placed at the 4 K stage. At room temperature, these rf signals are amplified by a heterostructure field effect transistor amplifier, mixed down to 10.7 MHz, and sampled by the digitizer. The resonant modes of the cavity and the antenna coupling are monitored by a vector network analyzer via the weak port and cavity bypass rf lines. A dilution refrigerator maintained an approximate temperature of 110 mK at the mixing chamber, enabling temperatures of 150 mK at the cavity and 120 mK at the JPA and circulators. Further details can be found in Ref. [38].

The power from axion conversion inside the cavity [27] is

$$P_{\text{axion}} = 7.7 \times 10^{-23} \text{ W} \left(\frac{V}{136\ell} \right) \left(\frac{B}{7.5 \text{ T}} \right)^2 \left(\frac{C}{0.4} \right) \times \left(\frac{g_\gamma}{0.36} \right)^2 \left(\frac{\rho_a}{0.45 \text{ GeV/cc}} \right) \left(\frac{f}{1 \text{ GHz}} \right) \left(\frac{Q_L}{80000} \right). \quad (1)$$

Here, V is the volume of the cavity, B is the magnitude of the magnetic field, C is the form factor representing the overlap between the cavity resonant mode and the magnetic field, g_γ is the model-dependent numerical constant -0.97 (0.36) for the KSVZ (DFSZ) model which determines, along with the axion decay constant f_a , the axion coupling to two photons $g_{a\gamma\gamma} = \alpha g_\gamma / \pi f_a$, ρ_a is the expected dark matter density in the cavity, f is the frequency of the photon induced by the axion field, and Q_L is the loaded quality factor of the cavity.

The signal-to-noise ratio (SNR) is used as a metric of the sensitivity of the experiment [39]:

$$\text{SNR} = \frac{P_{\text{axion}}}{k_B T_{\text{sys}} / \epsilon} \sqrt{\frac{t}{b}}, \quad (2)$$

where k_B is the Boltzmann constant, T_{sys} is the system noise temperature, which is defined as the sum of the physical and electronic noise temperatures, ϵ is the transmission efficiency between the cavity and the JPA, t is the integration time, and b is the detection bandwidth $b = f/Q_a \sim f/10^6$, the expected signal energy spread of nonrelativistic axion dark matter with a velocity of $\sim 10^{-3}c$.

T_{sys} is measured with the SNR improvement (SNRI) method. The SNRI is given by

$$\text{SNRI} = T_{\text{sys}}^{\text{off}} / T_{\text{sys}}^{\text{on}} = \frac{G_{\text{on}} P_{\text{off}}}{G_{\text{off}} P_{\text{on}}}, \quad (3)$$

where $G_{\text{on(off)}}$ and $P_{\text{on(off)}}$ are the total gain of the rf chain measured by the vector network analyzer and the power spectral density of the rf chain measured by the digitizer for the JPA in the on (off) state, respectively. As an over-coupled resonator, the JPA acts as a lossless mirror for the signal when the JPA is off. The SNRI was typically 7.5 dB. $T_{\text{sys}}^{\text{off}}$ is measured by the y-factor method [40] utilizing a noise source placed at the 500 mK stage (labeled as the ‘‘hot load’’). The hot load temperature, T_{hot} , can be varied between 0.5–4 K. During a y-factor measurement, the input of the cold receiver is connected to the hot load by flipping a switch in the receiver so that thermal photon from the hot load is detected. There is a linear relation between T_{hot} and the digitized power when the JPA is off:

$$P = G_{\text{off}} b k_B (T_{\text{hot}} \epsilon_h + T_{\text{sys}}^{\text{off}}). \quad (4)$$

Here, ϵ_h is the total transmission efficiency between the hot load and the JPA. Hence, one can obtain T_{off}/ϵ from the y-

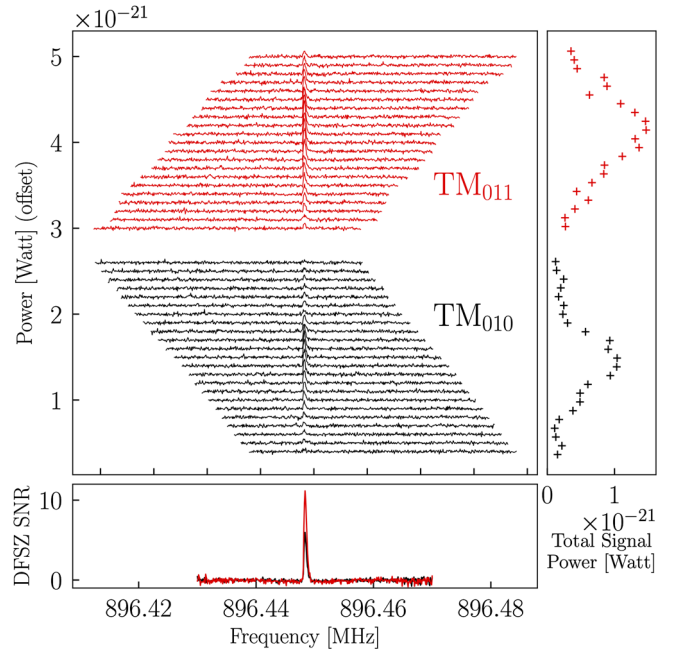


FIG. 2. Digitization spectra including a blinded SAG for TM_{010} (black) and TM_{011} (red) mode after removing the receiver shape and JPA standing wave distortion. The bottom small plot shows the combined SNR with respect to DFSZ power. The right small plot shows the integrated signal power and how it varies according to the Lorentzian cavity enhancement.

intersection of a linear fit. We assume ϵ_h is equal to ϵ since ϵ_h is dominated by losses in the circulators. During the data-taking period, T_{off}/ϵ was measured by the y-factor method every few months. The results were stable over time around 3.5 K, though they varied with frequency by 0.2 K over the frequency range. From the above, the typical T_{sys}/ϵ when the JPA is on was calculated to be 600 mK.

The data described here were acquired between October 2019 and May 2021. We aimed to probe axions with one (two) times DFSZ coupling between 950 and 1020 (800 and 950) MHz. Throughout the operation, synthetic axion generated signals (SAGs), which are created using lower power rf tones, were injected into the cavity via its weak port to ensure the robustness of the experiment. Two types of SAGs were injected: calibration SAGs, which were intended to verify the integrity of the receiver chain and analysis framework, and blinded SAGs to practice the full candidate evaluation procedure.

The explored frequency range was divided into 14 ‘‘nibbles,’’ narrow frequency ranges, typically 10 MHz in width. The specific procedure repeated for each nibble is as follows. First, digitizations for the entire nibble frequency range were performed by moving both tuning rods symmetrically. The integration time was 100 seconds. The spectral width was 50 kHz for each scan, and the data were averaged with 100 Hz bin resolution. Next, an analysis was performed to check for axionlike excesses (candidates) above the noise.

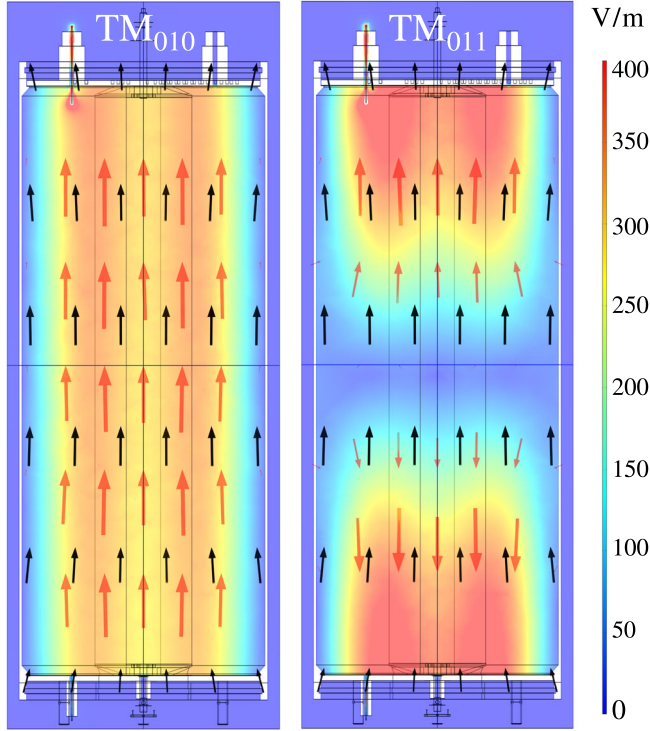


FIG. 3. Electric field distribution as a heat map for TM_{010} (left) and TM_{011} (right) modes simulated with COMSOL Multiphysics [42]. Electric field for the mode and impressed magnetic field are shown as red and black arrows, respectively. Calculated form factors with CST Magnetic Field Solver are 0.455 and < 0.001 for TM_{010} and TM_{011} modes, respectively. The overlap between the TM_{010} electric field and the magnetic field is large and consistent across the volume, while the overlap between the TM_{011} electric field is of opposite sign in the top and bottom of the cavity, leading to cancellations in the cavity response to the spatially uniform dark matter axion field.

The shape of the detected background is primarily determined by two factors: the shape generated by the room temperature receiver and the JPA standing wave due to the imperfect isolation of circulators, C_1 and C_2 . The former is time independent and was removed by a reference shape measured at the beginning of data taking. The latter varies when the bias current of the JPA is changed and was removed by a six-order Padé-approximant performed for each spectrum. The flattened spectra were scaled by the estimated T_{sys}/ϵ to obtain the correct power scale and were convolved with the expected axion shape to improve the sensitivity to axions. The spectra were coadded into a “grand spectrum” to make use of all recorded spectra. Typically, $\mathcal{O}(10)$ candidates are found within a nibble because of statistical fluctuations and calibration SAGs. The criteria to select candidates are described in Ref. [41]. Accordingly, the candidates were scanned further, a rescan, to check whether they are persistent. The rescan data are later included in the analysis, and a Monte Carlo study indicates that this procedure may induce a small bias of less than 3% on the resulting extracted axion-photon coupling

TABLE I. A list of candidates remaining after turning off calibration SAGs. The 896.448 MHz candidate was a blinded SAG. “Persistence” is checked when the candidate exists in all the scans with similar powers. “At same frequency” is checked when the candidate was at the given frequency ± 300 Hz. “Not in air” is flagged if the candidate could not be observed with a spectrum analyzer attached to an external antenna at the experimental site. “Enhanced on resonance” is flagged when the integral of the signal power was scaled as a Lorentzian function. “x” denotes tested but not passed.

Frequency [MHz]	Persistence	At same frequency	Not in air	Enhanced on resonance
839.669	✓	✗	✓	✗
840.268	✓	✓	✓	✗
860.000	✓	✓	✗	✗
891.070	✓	✓	✓	✗
896.448	✓	✓	✓	✓
974.989	✗	✓	✓	✗
974.999	✗	✓	✓	✗
960.000	✓	✓	✗	✗
980.000	✓	✓	✗	✗
990.000	✓	✓	✗	✗
990.031	✗	✓	✓	✗
1000.000	✓	✓	✗	✗
1000.013	✗	✓	✓	✗
1010.000	✓	✓	✗	✗
1020.000	✓	✓	✗	✗

limits in specific circumstances. After the first rescan, the calibration SAGs were turned off and the second rescan was performed to confirm whether the candidates were SAGs or true signals. If all SAGs were identified and there was no candidate left, then the data-taking moved on to the next nibble. However, if there still remained one or more candidates, more rigorous tests were performed as described below.

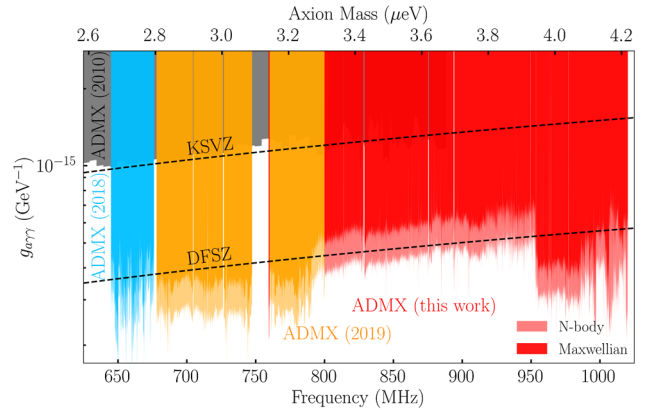


FIG. 4. 90% C.L. upper limits on $g_{a\gamma\gamma}$ as a function of axion mass. The gray-, blue-, and yellow-colored areas represent previous ADMX limits reported in Refs. [28,32,33]. The red-colored area shows the limits of this work. We ruled out KSVZ (DFSZ) axions in the 3.3–4.2 (3.9–4.1) μeV mass range.

A single candidate precipitated the full series of studies that is undertaken in the event of an axionlike signal, for which the final step would be a magnet ramp to check for B^2 scaling of the candidate signal power, as expected for an axion signal. Figure 2 shows the line shapes for the candidate. The candidate consistently emerged at the same frequency even though the cavity resonant frequency and digitization window were shifted. The frequency integrated power followed the expected Lorentzian line shape, consistent with the quality factor of the cavity. Therefore, it most likely originates inside the cavity. The individual line shapes followed the Maxwell-Boltzmann distribution exactly within the statistical uncertainty, as is expected from the standard halo model for dark matter.

A true axion signal should disappear when the TM_{011} mode is tuned to the candidate frequency because the electric fields are of the opposite polarity at the top and bottom of the cavity as shown in Fig. 3, so the form factor is almost zero. The candidate failed this test, and the magnet ramp was not applied. Therefore, the candidate was determined not to be consistent with the axion hypothesis and was subsequently revealed to be a blinded SAG.

Other than the blinded SAG, the analysis procedure detected 15 persistent candidates as summarized in Table I. None of the candidates passed the “enhanced on resonance” check except the blinded SAG described above. The other candidates did not pass the other criteria for being likely axion candidates. Therefore we are confident that these signals did not result from axion dark matter.

Upon eliminating all candidates in the frequency range of interest, we set 90% confidence level (C.L.) upper limits on the axion-photon couplings across the explored mass ranges with the assumption that axions make up 100% of the local dark matter density as shown in Fig. 4. We ruled out KSVZ (DFSZ) axions in the 3.3–4.2(3.9–4.1) μeV mass range. We initially aimed for DFSZ sensitivity overall (starting near the high-mass end of the energy range), but our system noise was suboptimal, making the scan speed much slower than we would like. Consequently, we decided to cover the remaining frequency range at two times DFSZ sensitivity (by scanning much more quickly) and then to upgrade the detector to reduce the system noise. The limits assumed that the velocity distribution of dark

TABLE II. Summary of uncertainties associated with the observed power.

Source	Fractional uncertainty on P_{axion}
Cavity Q factor	2%
Antenna coupling	2%
JPA SNRI	0.8%
T_{off}/ϵ	4.3%
B^2VC	3%
Total	6%

matter axions is either a boosted Maxwell-Boltzmann distribution [43] with dark matter density 0.45 GeV/cc or in accordance with an N -body simulation [44] with dark matter density 0.6 GeV/cc. The limits include systematic experimental uncertainties associated with the cavity, the amplifiers, and the electromagnetic field simulation as shown in Table II. The largest uncertainty was T_{off}/ϵ dominated by the temperature sensor accuracy. Additionally, a sensitivity loss from potential overfitting of signals from the Padé approximant used to remove distortions in the digitized spectra was taken into account. This effect was quantified by injecting software synthetic signals into the real data and comparing analysis results to the injected power. We determined that there was a 20% suppression of the axion power, i.e., $\sim 10\%$ loss of the axion-photon coupling.

Alternatively, we can set limits on the dark matter axion density with the assumption that the axion-photon coupling is given by the KSVZ model. This is shown in Fig. 5. The limit shows that KSVZ axions are excluded from contributing any more than 0.1 GeV/cc of the local dark matter density, or 20% of the expected density.

In summary, we searched for the “invisible” axion dark matter in the 3.3–4.2 μeV mass range. No axionlike excess was observed. Therefore, we set a limit for the axion-photon coupling that is the most stringent to date. We intend to rescan the region covered here (3.3–4.2 μeV) at DFSZ sensitivity after making a number of upgrades and repairs to the current cavity and rf system. These upgrades will include improving the thermal isolation of the cavity from the 1-K support to lower the overall heat load on the dilution refrigerator, upgrading the μ -metal shield to mitigate the remaining magnetic field on the JPA, and adding additional temperature sensors to measure the system noise temperature precisely.

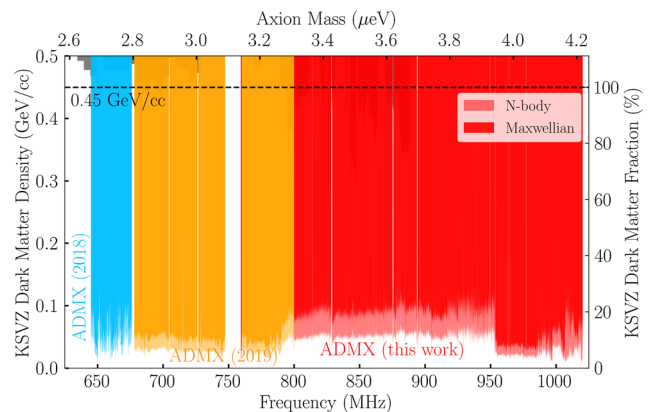


FIG. 5. 90% C.L. upper limits on the dark matter energy density assuming the KSVZ model for axion coupling. The blue- and yellow-colored areas represent previous ADMX limits reported in Refs. [32,33], respectively. The red-colored area shows the limits of this work. The KSVZ axions are excluded even though the axion density is 0.1 GeV/cc (20%) of the total dark matter density.

This work was supported by the U.S. Department of Energy through Grants No. DE-SC0009800, No. DESC0009723, No. DE-SC0010296, No. DE-SC0010280, No. DE-SC0011665, No. DEFG02-97ER41029, No. DEFG02-96ER40956, No. DEAC52-07NA27344, No. DEC03-76SF00098, and No. DE-SC0017987. Fermilab is a U.S. Department of Energy, Office of Science, HEP User Facility. Fermilab is managed by Fermi Research Alliance, LLC (FRA), acting under Contract No. DE-AC02-07CH11359. Additional support was provided by the Heising-Simons Foundation and by the Lawrence Livermore National Laboratory and Pacific Northwest National Laboratory LDRD offices. UWA participation is funded by the ARC Centre of Excellence for Engineered Quantum Systems, Grant No. CE170100009, Dark Matter Particle Physics, Grant No. CE200100008, and Forrest Research Foundation. The corresponding author is supported by JSPS Overseas Research Fellowships No. 202060305. LLNL Release No. LLNL-JRNL-826807.

*tnittal@uw.edu

- [1] P. Sikivie, *Rev. Mod. Phys.* **93**, 015004 (2021).
- [2] C. Abel *et al.*, *Phys. Rev. Lett.* **124**, 081803 (2020).
- [3] R. D. Peccei and H. R. Quinn, *Phys. Rev. Lett.* **38**, 1440 (1977).
- [4] S. Weinberg, *Phys. Rev. Lett.* **40**, 223 (1978).
- [5] F. Wilczek, *Phys. Rev. Lett.* **40**, 279 (1978).
- [6] J. Preskill, M. B. Wise, and F. Wilczek, *Phys. Lett.* **120B**, 127 (1983).
- [7] L. Abbott and P. Sikivie, *Phys. Lett.* **120B**, 133 (1983).
- [8] M. Dine and W. Fischler, *Phys. Lett.* **120B**, 137 (1983).
- [9] J. Ipser and P. Sikivie, *Phys. Rev. Lett.* **50**, 925 (1983).
- [10] S. Borsanyi, Z. Fodor, J. Guenther, K.-H. Kampert, S. D. Katz, T. Kawanai, T. G. Kovacs, S. W. Mages, A. Pasztor, F. Pittler, J. Redondo, A. Ringwald, and K. K. Szabo, *Nature (London)* **539**, 69 (2016).
- [11] M. Dine, P. Draper, L. Stephenson-Haskins, and D. Xu, *Phys. Rev. D* **96**, 095001 (2017).
- [12] T. Hiramatsu, M. Kawasaki, T. Sekiguchi, M. Yamaguchi, and J. Yokoyama, *Phys. Rev. D* **83**, 123531 (2011).
- [13] M. Kawasaki, K. Saikawa, and T. Sekiguchi, *Phys. Rev. D* **91**, 065014 (2015).
- [14] E. Berkowitz, M. I. Buchoff, and E. Rinaldi, *Phys. Rev. D* **92**, 034507 (2015).
- [15] L. Fleury and G. D. Moore, *J. Cosmol. Astropart. Phys.* **01** (2016) 004.
- [16] C. Bonati, M. D'Elia, M. Mariti, G. Martinelli, M. Mesiti, F. Negro, F. Sanfilippo, and G. Villadoro, *J. High Energy Phys.* **03** (2016) 155.
- [17] P. Petreczky, H.-P. Schadler, and S. Sharma, *Phys. Lett. B* **762**, 498 (2016).
- [18] G. Ballesteros, J. Redondo, A. Ringwald, and C. Tamarit, *Phys. Rev. Lett.* **118**, 071802 (2017).
- [19] V. B. Klaer and G. D. Moore, *J. Cosmol. Astropart. Phys.* **11** (2017) 049.
- [20] M. Buschmann, J. W. Foster, and B. R. Safdi, *Phys. Rev. Lett.* **124**, 161103 (2020).
- [21] M. Gorghetto, E. Hardy, and G. Villadoro, *SciPost Phys.* **10**, 50 (2021).
- [22] M. Buschmann, J. W. Foster, A. Hook, A. Peterson, D. E. Willcox, W. Zhang, and B. R. Safdi, [arXiv:2108.05368](https://arxiv.org/abs/2108.05368).
- [23] J. E. Kim, *Phys. Rev. Lett.* **43**, 103 (1979).
- [24] M. A. Shifman, A. Vainshtein, and V. I. Zakharov, *Nucl. Phys.* **B166**, 493 (1980).
- [25] M. Dine, W. Fischler, and M. Srednicki, *Phys. Lett.* **104B**, 199 (1981).
- [26] A. P. Zhitnitsky, *Sov. J. Nucl. Phys.* **31**, 260 (1980), <https://www.osti.gov/biblio/7063072>.
- [27] P. Sikivie, *Phys. Rev. Lett.* **51**, 1415 (1983).
- [28] S. Asztalos *et al.*, *Phys. Rev. D* **64**, 092003 (2001).
- [29] S. J. Asztalos, R. F. Bradley, L. Duffy, C. Hagmann, D. Kinion, D. M. Moltz, L. J. Rosenberg, P. Sikivie, W. Stoeffl, N. S. Sullivan, D. B. Tanner, K. van Bibber, and D. B. Yu, *Phys. Rev. D* **69**, 011101(R) (2004).
- [30] S. J. Asztalos, E. Daw, H. Peng, L. J. Rosenberg, D. B. Yu, C. Hagmann, D. Kinion, W. Stoeffl, K. van Bibber, J. LaVeigne, P. Sikivie, N. S. Sullivan, D. B. Tanner, F. Nezrick, and D. M. Moltz, *Astrophys. J.* **571**, L27 (2002).
- [31] S. J. Asztalos, G. Carosi, C. Hagmann, D. Kinion, K. van Bibber, M. Hotz, L. J. Rosenberg, G. Rybka, J. Hoskins, J. Hwang, P. Sikivie, D. B. Tanner, R. Bradley, and J. Clarke, *Phys. Rev. Lett.* **104**, 041301 (2010).
- [32] N. Du *et al.* (ADMX Collaboration), *Phys. Rev. Lett.* **120**, 151301 (2018).
- [33] T. Braine *et al.* (ADMX Collaboration), *Phys. Rev. Lett.* **124**, 101303 (2020).
- [34] J. E. Kim and G. Carosi, *Rev. Mod. Phys.* **82**, 557 (2010).
- [35] I. Siddiqi, R. Vijay, F. Pierre, C. M. Wilson, M. Metcalfe, C. Rigetti, L. Frunzio, and M. H. Devoret, *Phys. Rev. Lett.* **93**, 207002 (2004).
- [36] J. Aumentado, *IEEE Microw. Mag.* **21**, 45 (2020).
- [37] L. N. Factory, 0.6-2 ghz cryogenic low noise amplifier, https://www.lownoisefactory.com/files/1215/2585/7504/LNF-LNC0.6_2A.pdf.
- [38] R. Khatiwada *et al.*, [arXiv:2010.00169](https://arxiv.org/abs/2010.00169).
- [39] R. H. Dicke, *Rev. Sci. Instrum.* **17**, 268 (1946).
- [40] T. L. Wilson, [arXiv:1111.1183](https://arxiv.org/abs/1111.1183).
- [41] C. Bartram *et al.* (ADMX Collaboration), *Phys. Rev. D* **103**, 032002 (2021).
- [42] COSMOL AB, Comsol multiphysics v. 5.6., www.comsol.com.
- [43] M. S. Turner, *Phys. Rev. D* **42**, 3572 (1990).
- [44] E. W. Lentz, T. R. Quinn, L. J. Rosenberg, and M. J. Tremmel, *Astrophys. J.* **845**, 121 (2017).